CONFERENCE PRE-PRINT

TURBULENCE-TRANSPORT COUPLING SIMULATION STUDY OF THE ELM DYNAMICS FROM HIGH RECYCLING ATTACHED REGIME TO IMPURITY SEEDED DETACHMENT REGIME WITHIN EDGE PLASMA COUPLING SIMULATION (EPCS) FRAMEWORK

T.Y. LIU
School of Nuclear Science and Technology, University of Science and Technology of China
Hefei, P.R. China

T.H. HUANG
School of Nuclear Science and Technology, University of Science and Technology of China
Hefei, P.R. China

S.F. MAO
School of Nuclear Science and Technology, University of Science and Technology of China
Hefei, P.R. China

M.Y. YE
School of Nuclear Science and Technology, University of Science and Technology of China
Hefei, P.R. China
Email: yemy@ustc.edu.cn

Abstract

It is essential for future fusion reactors to achieve simultaneously divertor detachment and small or no edge-localized modes (ELMs), while maintaining high core plasma confinement. Divertor detachment evolves on transport timescales ($\gtrsim 10^{-3}$ s), and involves scrape-off layer transport and plasma-neutral interactions. In contrast, ELMs are governed by magnetohydrodynamic instabilities and nonlinear turbulence, occurring on much shorter Alfvén timescales ($\lesssim 10^{-6}$ s). Investigating the compatibility between these phenomena requires integrated simulation of edge plasma turbulence and profile evolution across disparate timescales. For predicting the edge plasma behaviour in future fusion reactors, self-consistent turbulence-transport coupling simulation is essential. Using the Edge Plasma Coupling Simulation framework, the influence of divertor operational states on ELM behaviour under neon impurity seeding is investigated in this work, based on the EAST experiment on that achieved detachment with small ELMs. Simulations show that increased neon concentration facilitates a transition to detachment, accompanied by a reduction in ELM amplitude and an increase in ELM frequency, consistent with experimental observations. Further analysis indicates that neon induced modifications to the pedestal profile suppress peeling-ballooning mode instabilities. Statistical analysis of turbulent transport fluxes reveals that a weakened anticorrelation between flux and profile gradients under neon seeding is the key mechanism driving the transition from large to small ELMs.

1. INTRODUCTION

Effective control of first wall heat load poses a critical challenge for steady-state operation in future fusion reactors. On one hand, the divertor target must withstand substantial steady-state heat flux in high confinement mode (H-mode). On the other hand, periodic edge-localized modes (ELMs) during H-mode can induce enormous transient heat and particle fluxes from the core confinement region within extremely short timescales, imposing significant transient thermal loads on both divertor targets and the main chamber. To address these challenges, future reactors need to achieve divertor detachment through impurity seeding to reduce steady-state heat/particle fluxes, while simultaneously implementing effective ELM control strategies to achieve small/no ELM regime for transient heat load mitigation. These requirements must be compatible with maintaining high core confinement performance.

Significant interactions exist between divertor operational states and pedestal ELM dynamics. Large ELMs can periodically disrupt the “gas cushion” required for divertor detachment through intense thermal/particle fluxes (burning through effect), whereas small ELMs (e.g., grassy ELMs) with enhanced turbulent transport may facilitate detachment at lower densities. Conversely, achieving detachment through increasing scrape-off layer

(SOL) density reduces pedestal density gradients, promoting small/no-ELM operation. Impurity seeding not only facilitates radiative detachment but also significantly influences pedestal turbulence and ELM dynamics. Understanding these interactions is crucial for steady-state operation. Despite existing computational tools for transport modeling (such as SOLPS-ITER [1] etc.) and for turbulence simulations (such as BOUT++ [2] etc.), self-consistent simulations of edge plasma evolution to the transport timescale remain challenging.

A turbulence-transport code coupling approach offers a solution for efficient and accurate long-term self-consistent simulations. In our previous work, the Edge Plasma Coupling Simulation (EPCS) framework is developed [3], which is consisted of various components to provide the interfaces for the specified turbulence and transport codes (BOUT++ and SOLPS-ITER at present stage), the data transfer interfaces between the turbulence and transport code, the code running drivers and the function for configuration of the specified coupling simulation workflow. Using EPCS, both steady-state and time-dependent coupling workflows have been developed and successfully applied for simulating EAST discharges. Based on the EAST experiment achieving compatible divertor detachment and small ELMs via neon injection, this work applies the time-dependent coupling workflow to simulate the edge plasma self-consistently across varying neon impurity concentrations.

2. SIMULATION SETUPS

In EAST Shot #114688, compatible operation of divertor detachment with small ELMs is achieved by neon impurity injection under a lower single-null configuration. The magnetic field was in an "unfavourable" configuration, meaning the $B\times\nabla B$ direction points away from the X-point. Plasma current I_p = 550 kA, toroidal magnetic field B_t = 2.14 T, safety factor $q_{95} \approx 4$. Total heating power P_{total} = 7.4 MW (including 5 MW of neutral beam injection, 1 MW of lower hybrid wave heating, and 1.4 MW of ion cyclotron resonance heating) and total absorbed power P_{abs} = 3.9 MW. After neon impurity injection at 3.5 s, the ELM amplitude significantly decreased, and the ELM frequency increased (from 200 Hz to 500 Hz). Plasma density increased, and plasma stored energy rose. The electron temperature T_{et} at the inner divertor target plate remained at a relatively low level of about 5 eV, and the ion saturation current decreased, entering a particle-detached state; the electron temperature T_{et} at the outer target plate dropped below 5 eV, while the ion saturation current remained basically unchanged, indicating an energy-detached state.

The simulation uses the MHD equilibrium configuration from this shot before impurity injection at t = 3.3 s. Fig. 1 shows the flux surface-aligned grids used by the SOLPS-ITER code (red) and the BOUT++ code (black). The computational domain covers the pedestal region and the SOL, with the normalized poloidal magnetic flux ψ ranging from 0.80 to 1.05. The radial-poloidal resolution of the BOUT++ grid is 256×64, while that of the SOLPS-ITER grid is 36×96, and the BOUT++ grid additionally includes 64 grid units in the toroidal direction.

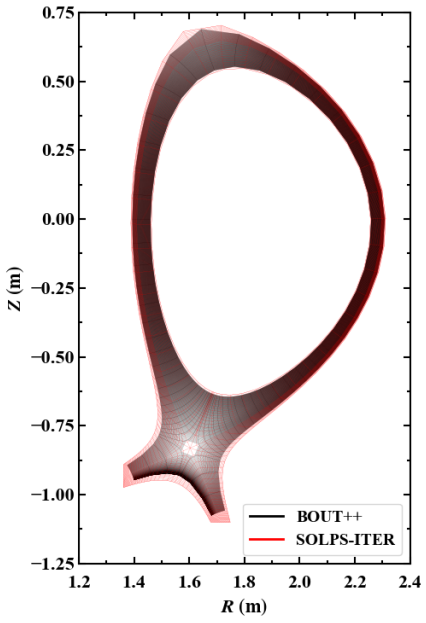

FIG. 1. Computational grids for SOLPS-ITER (red) and BOUT++ (black).

SOLPS-ITER uses a full current and drift model, with the ion density n_i fixed at 3.4×10^{19} m^{-3} at the core-edge interface (CEI). Total power across CEI is set as 3 MW, equally shared between electrons and ions. The boundary conditions at the inner and outer targets are sheath boundary conditions. The impurity distribution is calculated by SOLPS-ITER. Since SOLPS-ITER currently lacks a model for SMBI injection, and to accelerate the coupling simulation process, impurities are introduced by adjusting the density of Ne^{8+} at the CEI. BOUT++ uses a six-field two-fluid model, considering the impurity effect of Ne^{8+} in the vorticity equation [4].

The simulation adopts the time-dependent coupling simulation workflow from the EPCS framework. While the computational efficiency can be improved by performing the turbulence simulation within its characteristic time, the self-consistency between the plasma transport and the turbulence flux is ensured by the inner iteration (controlled by internal iteration error tolerance) within a transport time step based on the predictor-corrector method. The adaptive variable time step algorithm is adopted to control the relative error during fast-changing ELM phase and improve the efficiency during the slow-changing recovery phase. The RUN_TRANS module extracts plasma profiles from SOLPS-ITER, including: main ion density n_i, Ne^{8+} density n_{imp}, electron density n_e, ion temperature T_i, electron temperature T_e, total pressure P, parallel current $J_\parallel$, and electric potential ϕ. SOLPS-ITER's physical model uses the total ion internal energy equation, assuming sufficient heat exchange between different ion species. Therefore, the impurity ion temperature is considered consistent with the main ion temperature.

The RUN_TURB module extracts the effective particle diffusion coefficient D_i, effective velocity V, and effective ion/electron thermal diffusion coefficients χ_i/χ_e from BOUT++. These coefficients are obtained by calculating the radial flux transport flows. In this work, it is preliminarily assumed that the impurity particle diffusion coefficient D_{imp} and thermal diffusion coefficient χ_{imp} are consistent with those of the main ions.

Based on the experimental profiles, the initial profiles used in the coupling simulation are shown in Fig. 2. Since the initial profile is in a large ELM phase with high instability, the initial turbulence simulation cannot evolve to a quasi-steady saturated state. Therefore, the RUN_TURB module starts the turbulence simulation with random small initial perturbations.

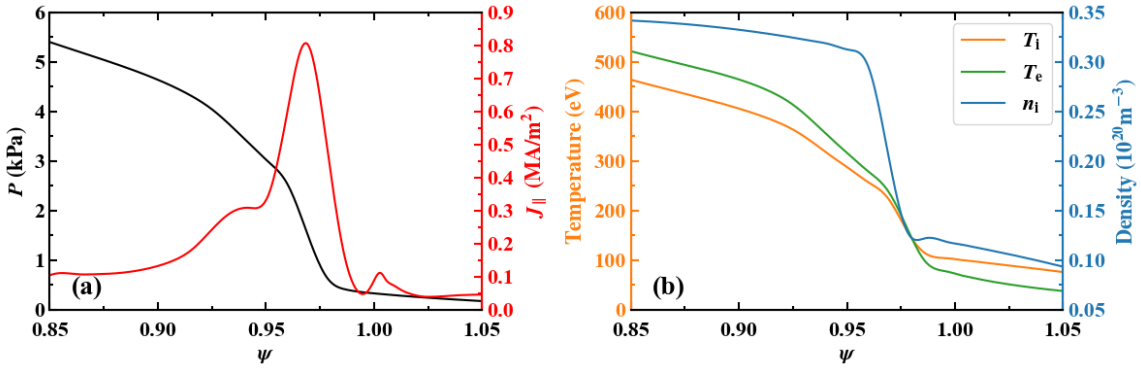

FIG. 2. Plasma profiles at the outer midplane used for the simulation; (a) pressure (black) and parallel current density (red) profiles; (b) ion density (blue), ion temperature (orange), and electron temperature (green) profiles.

3. SIMULATION RESULTS

As shown in Fig. 3, the time-dependent coupling simulation is divided into three stages:

(1) Stage 1 (0 ~ 22.5 ms): Starting with no impurity injection, Fig. 3 (b) shows three sharp increases in the electron temperature at the outer target (OT) strike point caused by ELM transient heat fluxes, with the peak temperature around 50 eV. During inter-ELM periods, the strike point temperature is about 30 eV. Therefore, this stage corresponds to the operational phase of large ELMs and an attached divertor (Phase A).

(2) Stage 2 (22.5 ~ 46.7 ms): At t = 22.5 ms, the density of Ne^{8+} at the CEI is fixed at 5×10^{17} m^{-3}. From Fig. 3 (a), it can be seen that after t = 39 ms, the neon impurity gradually forms a relatively stable distribution in the upstream. Meanwhile, after experiencing significant perturbations, the strike point electron temperature eventually stabilizes

around 25 eV. The electron temperature shows periodic perturbations at this stage, but their amplitude is significantly reduced compared to Stage 1. Therefore, the period t = 39 ~ 46.7 ms can be considered as the operational phase of small ELMs and an attached divertor (Phase B).

(3) Stage 3 (46.7 ~ 65 ms): Since the divertor remains attached, at t = 46.7 ms, the Ne^{8+} density at the CEI is further increased to 1×10^{18} m^{-3}. It can be observed that after t = 56 ms, while the neon impurity forms a relatively stable distribution in the upstream, the strike point electron temperature drops to about 5 eV, and its periodic perturbations become difficult to observe. Combined with the following analysis, the period t = 56 ~ 65 ms can be considered as the operational phase of small ELMs and a detached divertor (Phase C).

It should be noted that since the initial turbulence simulation starts from random small perturbations, the time-dependent coupling simulation experiences a long numerical transient process. Therefore, the time t = 0 ms is not the start of the coupling simulation, but rather the moment when the first large ELM begins.

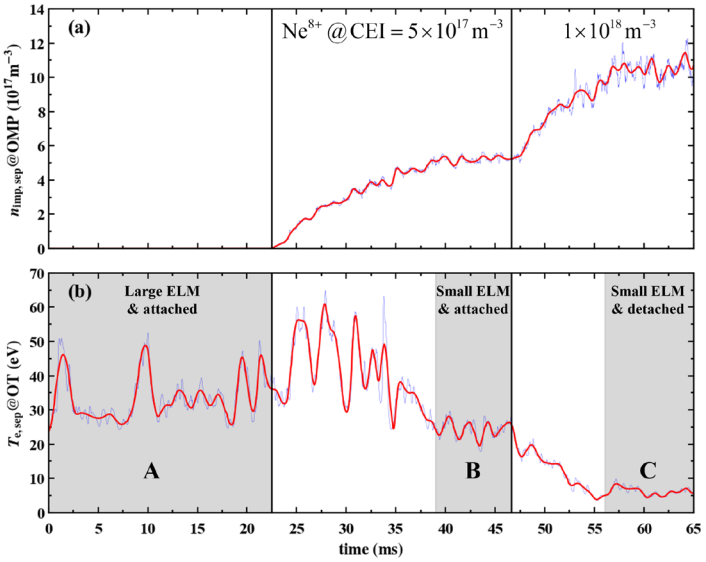

FIG. 3. (a) Time evolution of the impurity ion density Ne^{8+} at the separatrix of the outer midplane (OMP) and (b) electron temperature at the outer target (OT) strike point. The blue curve is the raw simulation data, the red curve is the low-pass filtered curve. The black vertical lines indicate the start times of impurity injection at 22.5/46.7 ms, the impurity ion density Ne^{8+} at the core-edge interface (CEI) is fixed at $5\times10^{17}/1\times10^{18}$ m^{-3}. The gray areas represent different operational phases: A t = 0.0 ~ 22.5 ms large ELM & attached, B t = 39 ~ 46.7 ms small ELM & attached, C t = 56 ~ 65 ms small ELM & detached.

From the particle and heat flux distributions at the target plates (Fig. 4), it can be seen that compared to Phase A without impurity injection (red line), Phase C (blue line) shows a significant reduction in both the main ion particle flux and the total heat flux in the inner and outer divertor. In phase C, both inner and outer targets are in an energy-detached state. Meanwhile, the degree of particle detachment at the inner target is higher than that at the outer target, a characteristic that is qualitatively consistent with the experimental results. As the divertor gradually enters a detached state, the region of concentrated neon (Ne) impurity radiation migrates from near the outer divertor strike point (Fig. 5 (a)) towards the X-point (Fig. 5 (b)). Under the detached divertor state (Phase C), the total radiation power from Ne impurities within the simulation region reaches 2.39 MW, accounting for about 80% of the total input power. Among this total radiation power, the contribution from the core confinement region is 0.68 MW, accounting for about 28%.

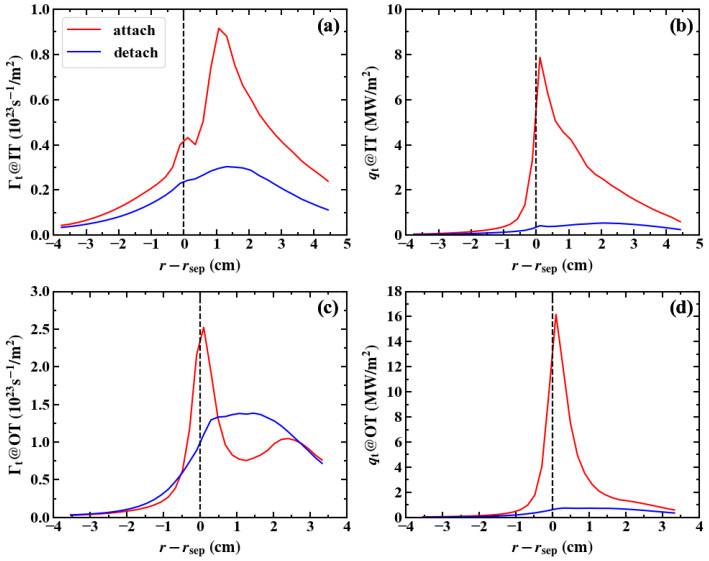

FIG. 4. Time-averaged distributions of main ion particle flux density and total heat flux density along the radial distance of the target plate for the inner (IT) and outer (OT) divertors. The red line represents Phase A, the blue line represents Phase C.

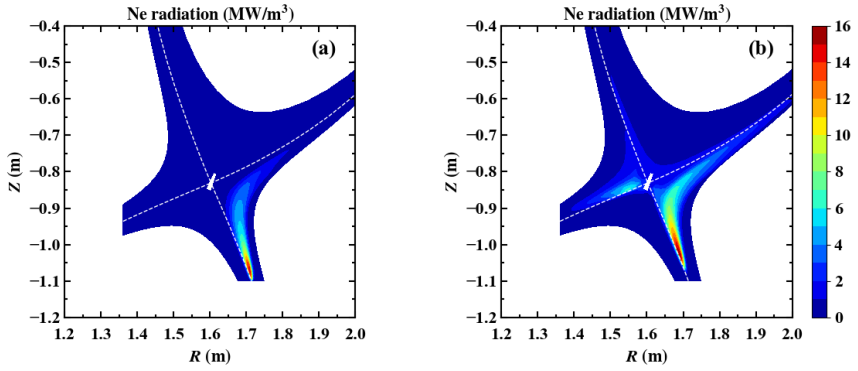

FIG. 5. Time-averaged Ne radiation power density distributions in the divertor region for (a) attached (Phase B) and (b) detached (Phase C) states. Total radiation power (a) 1.03 MW, (b) 2.39 MW; confinement region radiation power (a) 0.24 MW, (b) 0.68 MW.

To study the ELM process in different operational phases, three ELMs were selected from the large ELM phase (Phase A) and the small ELM phase (Phase C), as shown in Fig. 6. For each ELM event, two characteristic times are selected: pre-ELM and post-ELM. Here, pre-ELM is the moment just before the ELM crash, when the pressure gradient in the pedestal region reaches its maximum, and the separatrix pressure drops to a minimum. Post-ELM is the moment immediately after the ELM crash ends, when the crash has significantly reduced the pedestal pressure gradient and removed some particles and energy from the pedestal, causing the separatrix pressure to rise to a maximum. The period from pre-ELM to post-ELM is called intra-ELM. After the ELM crash ends, the pedestal enters a slow recovery phase, where the pedestal pressure gradient gradually increases, and the separatrix pressure correspondingly decreases until the next ELM crash. The period from post-ELM to the next pre-ELM is called inter-ELM. From Fig. 6, it can be seen that after a large ELM crash, it quickly enters the pedestal recovery phase. In contrast, the small ELM crash process exhibits quasi-continuous exhaust characteristics, and its pressure profile remains altered for a relatively long time after the crash before entering the recovery phase. This characteristic makes accurately determining the post-ELM time for small ELMs very difficult. Therefore, this work defines the post-ELM time as the midpoint between the pre-ELM times of two consecutive small ELMs.

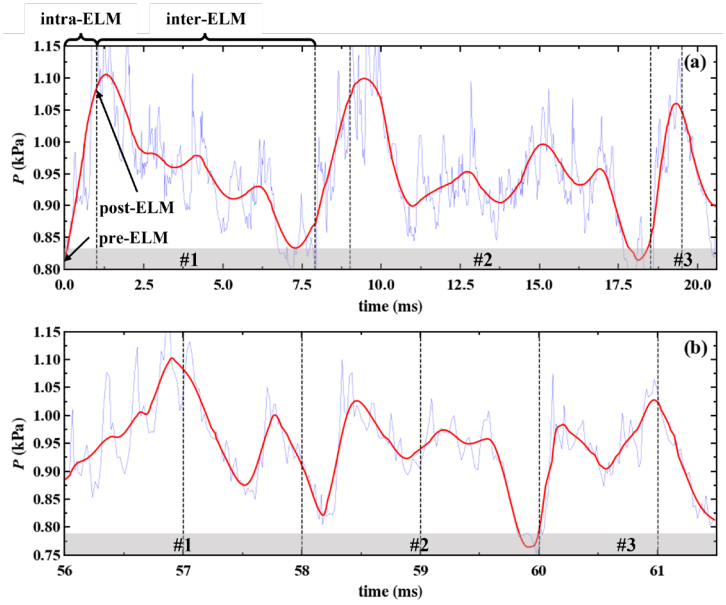

FIG. 6. (a) Large ELM (Phase A) and (b) small ELM (Phase C) evolution of the flux-surface averaged pressure at the separatrix. The blue curve is the raw simulation data, the red curve is the low-pass filtered curve. Three ELM events are selected for each operational phase, labeled #1, #2, and #3. For each ELM, the pre-ELM and post-ELM times are selected, indicated by dashed lines. Each ELM includes the intra-ELM phase from pre-ELM to post-ELM and the inter-ELM phase after post-ELM.

In the large ELM phase (Phase A), the average time interval between different pre-ELM/post-ELM pairs is 9.25 ms, corresponding to an ELM frequency of approximately 108 Hz. This frequency is lower than the experimentally observed ELM frequency of about 200 Hz. In the small ELM phase (Phase C), the average time interval between different pre-ELM/post-ELM pairs is 2 ms, corresponding to an ELM frequency of 500 Hz, consistent with the small ELM frequency observed after impurity injection in the experiment. It is worth noting that experiments typically involve consecutive discharges, which may lead to residual impurities from previous shots. This might be the reason why some ELM mitigation is observed even without impurity injection in the experiment. From Fig. 6, it can be seen that in the large ELM phase, the average duration of inter-ELM is about 8 ms, much longer than the average duration of intra-ELM (about 1 ms). In the small ELM phase, although the average duration of intra-ELM is comparable to that in the large ELM phase, the amplitude of the pressure perturbation is significantly reduced. This allows for faster pedestal recovery after the small ELM crash, resulting in a shortened average inter-ELM duration to about 1 ms, similar to the intra-ELM duration.

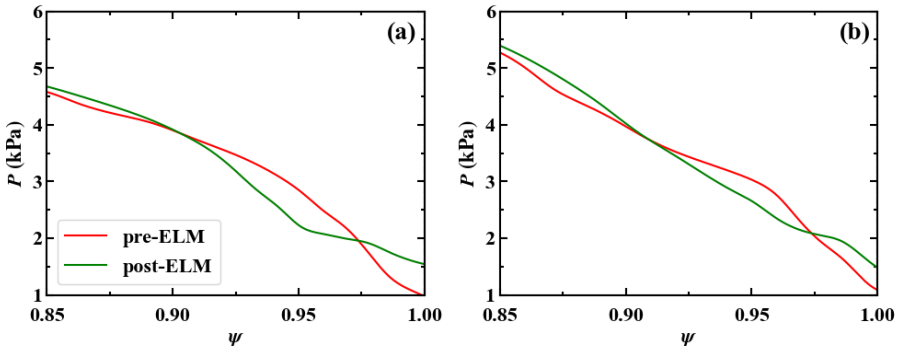

FIG. 7. Radial total pressure profiles at the outer midplane at the pre-ELM (red line) and post-ELM (green line) times for (a) large ELM #1 and (b) small ELM #3. ELM size: (a) 4.75%, (b) 2.53%.

Fig. 7 shows the evolution of the total pressure profile at the outer midplane for a typical large ELM (#1) and a small ELM (#3). The red/green lines represent the profiles at the pre-ELM/post-ELM times. It can be seen that although the small ELM has a higher pressure at the pre-ELM time, the degree of its pressure profile collapse is

smaller than that of the large ELM. The ELM size for the large ELM is about 4.75%, while for the small ELM it is about 2.53%, reduced by about half compared to the large ELM.

4. DISCUSSION

Fig. 8 shows the profile changes at the outer midplane for the attached (red) and detached (blue) states. It can be seen that when impurity injection achieves divertor detachment, due to the ionization of impurity particles, the electron density in the pedestal (Fig. 8 (b)) increases significantly compared to the attached state. The density at the pedestal top (ψ = 0.85 ~ 0.95) approaches the experimental measurement values from reflectometry. The increase in electron density at the separatrix is relatively small, and the electron density gradient increases, qualitatively consistent with experimental results. However, the simulated separatrix density differs from the experiment. The experimentally measured separatrix electron density is lower, and the density gradient is larger. This may be related to the lithium wall conditioning in the experiment – lithium reduces particle recycling from the wall, while the simulation uses a 100% recycling rate setting and does not consider the effect of wall conditioning. Compared to the electron density, the change in the main ion density (Fig. 8 (a)) at the pedestal top during detachment is relatively small, while the main ion density near the separatrix decreases more significantly, and the pedestal density gradient increases slightly. Due to impurity radiation, the electron temperature at the pedestal top (Fig. 8 (d)) decreases significantly, while the electron temperature at the separatrix remains basically unchanged, and the pedestal temperature gradient decreases, qualitatively consistent with the electron temperature changes measured by Thomson scattering. The ion temperature (Fig. 8 (c)) changes relatively little at the pedestal top during detachment, but increases significantly in the steep gradient region (ψ = 0.95 ~ 1.00), and the temperature gradient decreases significantly.

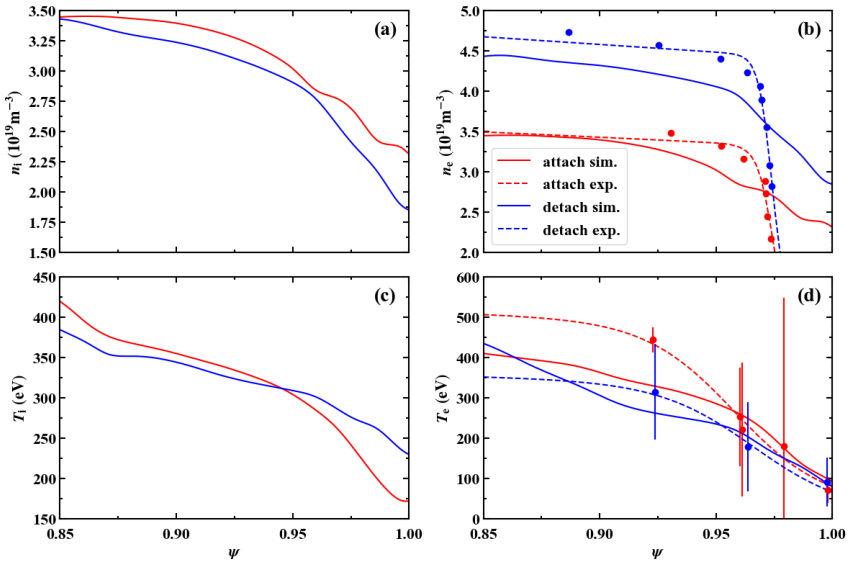

FIG. 8. Radial profiles at the outer midplane of (a) main ion density, (b) electron density, (c) ion temperature, and (d) electron temperature. Red represents the attached state at t = 0 ms, blue represents the detached state at t = 60 ms. Dots are experimental measurement data during the attached (red) and detached (blue) phases, dashed lines are fits to the experimental data. Due to lack of diagnostics in the pedestal region, there is no experimental data for main ion density and ion temperature. Error bars are shown for the electron temperature measurements.

The changes in profiles after impurity injection significantly affect pedestal instability. As shown in Fig. 9, at the pre-ELM, the linear growth rates for all toroidal mode numbers *n* for the small ELM (blue) show a clear reduction compared to the large ELM (red), except for the *n* = 5 mode which itself has a low growth rate. The small ELM growth rates are comparable to those at the post-ELM of the large ELM crash (green). The red dashed line shows the large ELM growth rate with the additional consideration of the Ne^{8+} impurity ion distribution from the small ELM. It can be seen that impurities can stabilize the linear growth of large ELMs, but compared to the profile changes, impurities play a secondary role in stabilizing the linear growth rate from large to small ELMs.

Based on a phenomenological model of ELM cycles [5], ELM size has a significant relationship with turbulent transport, which will be further discussed in detail at the conference.

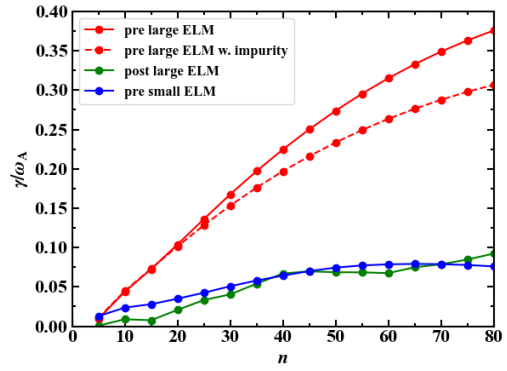

FIG. 9. Linear growth rates for different toroidal mode numbers n. Red solid line: large ELM #1 at pre-ELM time (t = 0 ms). Green solid line: large ELM #1 at post-ELM time (t = 1 ms). Blue solid line: small ELM #3 at pre-ELM time (t = 60 ms). Red dashed line: large ELM #1 at pre-ELM time (t = 0 ms) but additionally considering the distribution of Ne^{8+} impurity ions from small ELM #3 at pre-ELM time (t = 60 ms).

5. SUMMARY

Aimed at EAST experiments where neon injection achieved compatible divertor detachment with small ELMs, a simulation study was conducted on how the divertor state affects ELM behaviour under neon seeding. The simulation results show that as the neon impurity concentration increases, the divertor state changes from attached to detached, while the ELM amplitude decreases and the frequency increases, consistent with the experimental observations of divertor state change and the transition from large to small ELMs after neon impurity injection. The simulated large ELM frequency is about 108 Hz, lower than the experimental value (~200 Hz); the small ELM frequency is about 500 Hz, consistent with the experiment. Analysis indicates that significant changes in pedestal profiles due to impurity seeding can strongly suppress peeling-ballooning mode instabilities. The statistical analysis of turbulent transport fluxes under different divertor states indicates that the reduction in the anticorrelation between the turbulent transport flux and the absolute value of the profile gradient under neon impurity injection is the key physical mechanism for the transition from large ELMs to small ELMs.

ACKNOWLEDGEMENTS

This work is supported by the National MCF Energy R&D Program of China (Grant No. 2019YFE03030004, 2024YFE03010003, 2019YFE03080500), the National Natural Science Foundation of China (Grant No. 11975232). The results are obtained with the help of the EIRENE package (see www.eirene.de) including the related code, data and tools [1]. Numerical simulations are carried out using the CFETR Integration Design Platform (CIDP) with the support of the Supercomputing Center of University of Science and Technology of China.

REFERENCES

[1] Reiter D, Baelmans M, Börner P. The EIRENE and B2-EIRENE Codes[J]. Fusion Science and Technology, 2005, 47(2): 172-186.
[2] XIA T Y, XU X Q, XI P W. Six-field two-fluid simulations of peeling–ballooning modes using bout++[J]. Nuclear Fusion, 2013, 53(7): 073009.
[3] LIU T Y, HUANG T H, MAO S F, et al. Development of a code interface for coupled turbulence-transport simulations of tokamak edge plasmas[J]. Plasma Physics and Controlled Fusion, 2025, 67(5): 055004.
[4] LI Z Y, CHEN X, MUSCATELLO C M, et al. Numerical modelling of pedestal stability and broadband turbulence of wide-pedestal QH-mode plasmas on DIII-D[J]. Nuclear Fusion, 2022, 62(7): 076033.
[5] LEBEDEV V B, DIAMOND P H, GRUZINOVA I, et al. A minimal dynamical model of edge localized mode phenomena[J]. Physics of Plasmas, 1995, 2(9): 3345-3359.